

slope of the light curves, and hence require more nickel to power the late light curve. Decreasing the velocity boosts the late luminosity, and can reproduce the observed line shapes. However, these velocities were not predicted by the models that fit the early spectrum and light curve.

4. Conclusions

The monitoring of SN 1998bw through its second year has provided important new clues on the nature of this object. The late spectrum very much resembles the ones of other Type Ib/c supernovae. Hence, SN 1998bw can be tied to a class of objects we know fairly well. We confirm the large nickel mass required to power the optical radiation of this event, but find discrepancies by fitting the late spectrum with the models which were used to interpret the early phases. The implied energies are still unique for any supernova ever observed.

The connection of SN 1998bw to GRB980425 is still unclear, but we do not expect to see any signature of the burst at these late phases. The radio observations have been linked to the γ -ray burst and the relativistic expansion of material (Kulkarni et al. 1998, Li & Chevalier 1999). The X-ray emission from the GRB afterglow is coincident with the supernova as well (Pian et al. 1999). SN 1998bw remains a fascinating and puzzling object.

The combination of two instruments and telescopes to follow SN 1998bw to late phases has been very useful. The 3.6-m/EFOSC2 provided the early coverage and only at the end was the supernova 'handed' to UT1/FORS1. We were therefore able to secure a spectrum about every month and could follow this object further than would have been possible with the 3.6-m.

It is unlikely that there will be a third observing season for SN 1998bw. Unless the luminosity becomes constant, it will be too faint to be recovered.

There are known processes that could lead to such a constant flux, e.g. interaction with the circumstellar material or input from the accretion on a black hole. We have been following several such objects already and SN 1998bw will be worth at least a check in the next few months.

References

- Galama, T.J., et al. 1998, *Nature*, **395**, 670.
 Höflich, P., Wheeler, J. C., & Wang, L. 1999, *ApJ*, **521**, 179.
 Iwamoto, K., et al. 1998, *Nature*, **395**, 672.
 Kulkarni, S.R., et al. 1998, *Nature*, **395**, 663.
 McKenzie, E. H. & Schaefer, B.E. 1999, *PASP*, **111**, 964.
 Li, Z.-Y. & Chevalier, R.A. 1999, *ApJ*, **526**, 716.
 Patat, F., et al. 2000, in preparation.
 Pian, E., et al. 1999, *A&ASS*, 138, 463.
 Sollerman, J., et al. 2000, *ApJ*, submitted.
 Woosley, S.E. 1993, *ApJ*, **405**, 273.
 Woosley, S. E., Eastman, R.G., & Schmidt, B.P. 1999, *ApJ*, **516**, 788.

MISTRAL: Myopic Deconvolution Method Applied to ADONIS and to Simulated VLT-NAOS Images

Jean-Marc Conan¹, Thierry Fusco¹, Laurent M. Mugnier¹, Franck Marchis²

¹ONERA, Département d'Optique Théorique et Appliquée, France ([name](mailto:{name}@onera.fr)@onera.fr);

²ESO, Santiago, Chile (fmarchis@eso.org)

1. Introduction

The performance of high-resolution imaging with large astronomical telescopes is severely limited by the atmospheric turbulence. Adaptive optics [1, 2, 3] (AO) offers a real-time compensation of the turbulence. The correction is however only partial [2, 4, 5, 6, 7] and the long-exposure images must be deconvolved to restore the fine details of the object.

Great care must be taken in the deconvolution process if one wants to obtain a reliable restoration with good photometric precision. Two aspects add to the difficulty: the fact that the residual point spread function (PSF) is usually not perfectly known [8, 9, 10], and the fact that astronomical objects are usually a mix of sharp structures and smooth areas. "MISTRAL" (Myopic Iterative STep Preserving ALgorithm) [11, 8] has been developed to account for these two points. It is based on a rigorous Bayesian approach which allows us to easily account for the noise in the image, the imprecise knowledge of the PSF, and the available *a priori* information on the object (spatial structure, positivity...). A specific edge preserving object prior is proposed, which is in particular well adapted for planetary-like objects.

The notion of AO partial correction is first discussed in Section 2. The principle of our deconvolution technique is briefly summarised in Section 3. In Section 4, the photometric accuracy of MISTRAL is first demonstrated on simulated AO images. The simulation parameters correspond to NAOS, the AO system of the VLT. MISTRAL is then applied to ADONIS images of Io taken at thermal wavelengths using the COMIC camera. This allows an accurate mapping of Io's surface volcanic activity. We also used our deconvolution method on broadband filter (J, H, K) images of Uranus taken with SHARPII+. The structures of the rings and its innermost satellites have been successfully detected.

2. Partially Corrected AO Images

Within the isoplanatic angle, the intensity $i(r)$ at the focal plane of the system consisting of the atmosphere, of the telescope and of the AO bench is given by:

$$\mathbf{i}(r) = \mathbf{h}(r) * \mathbf{o}(r) + \mathbf{n}(r), \quad (1)$$

where r is the spatial coordinate, $\mathbf{o}(r)$ is the observed object, $\mathbf{h}(r)$ is the system PSF and $\mathbf{n}(r)$ is an additive zero mean noise.

We consider here the case of AO corrected long exposure images. Such an image is presented in Figure 1. In this numerical simulation, we considered an 11th magnitude planetary-like object observed in the visible with the NAOS AO system [12] installed on the VLT. This system will provide high performance in the near IR ($SR \approx 70\%$ at high flux). Here we consider the case of observations at visible wavelength ($\lambda = 0.5 \mu\text{m}$). In such conditions, the image blur is very severe, the expected SR is only 2.1% for a 0.73 arcsec seeing. Neither the fine structures on the surface of the object, nor the stars in the background are apparent in the corrected image. A deconvolution is therefore required.

The deconvolution procedure needs a measurement of the PSF. The usual procedure consists in recording the corrected image of a nearby unresolved star shortly after observing the object of interest. Since the correction quality depends on the observing conditions (turbulence strength, magnitude of the source used for wavefront sensing), the unresolved star image is not a perfect measurement of the PSF associated with the image to be deconvolved [8, 11, 13, 14]. Actually, the main source of PSF variability is the seeing fluctuation.

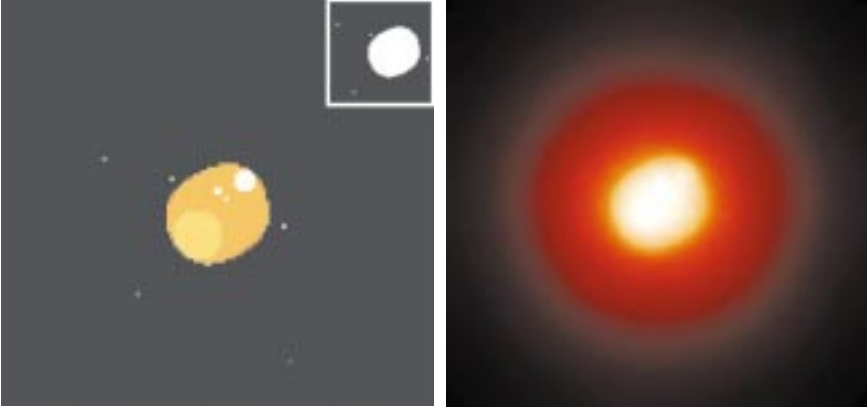


Figure 1: Planetary-type object ($m_v = 11$) and its simulated VLT-NAOS image at $0.5 \mu\text{m}$ and for a 0.73 arcsec seeing. The Strehl Ratio (SR) is 2.1%. The number of detected photons in the image is $10^8 \text{ photo} - e^-$, the background noise has a $31 e^-$ standard deviation. The Field of View is 0.8 arcsec , $128 \times 128 \text{ pixel}$ image. The planetary disk is constituted of a uniform level plus a broad feature 10% brighter, and three small spots, 30% brighter. Four stars are added in the field with a 2.5 magnitude difference between the brightest and the faintest. The faintest corresponds to 40,000 detected photons, which corresponds to a maximum contribution of 155 photons/pixel in the image. The true object top-right display gives a log-scale representation.

The sensibility of the Optical Transfer Function (OTF) to the seeing variations is illustrated in Figure 2. The OTFs are estimated for a seeing ranging from 0.65 to 0.93 arcsec. The corresponding SRs go from 3.8% down to 0.4%. The structure of the OTFs is typical of an AO corrected OTF [4, 5, 6, 7]: a low-frequency lobe and a high-frequency wing going up to the telescope cut-off frequency. The spatial frequencies between r_o/λ and D/λ , which would be lost without correction, are now preserved. The high-frequency level is however low and very dependent of the seeing conditions. Here it changes by a factor of ten for rather realistic seeing changes.

The OTFs presented here derive from a careful study of the system performance [12, 15]. The corresponding PSF at 0.73 arcsec seeing is shown in Figure 3. Note that despite the very low SR in the visible, a coherent peak is still clearly seen above the broad halo. This is characteristic of high-order correction systems such as the VLT-NAOS one working in the visible: the residual phase variance is large due to the short wavelength, but the phase is mainly constituted of high-order modes, hence the particular PSF profile. We will show in Section 4 that MISTRAL can restore high-resolution maps out of these low SR visible VLT-NAOS images. Note that this suggests that the SR is not a good measurement of the image quality, when quality means "restorability" [7].

Of course, the deconvolution can also be applied to IR images with more reasonable SRs as shown on ADONIS data in Section 5. But we first recall the deconvolution approach in the following section.

3. Deconvolution Approach

Most deconvolution techniques boil down to the minimisation (or maximisa-

tion) of a criterion. The first issue is the definition of a suitable criterion for the given inverse problem. The criteria presented here will be derived from a probabilistic approach. The second problem is then to find the position of the criterion's global minimum which is defined as the solution. In some cases, it is given by an analytical expression, but most of the time one has to use an iterative numerical method to solve the problem.

In the following sections, we first consider the case of an assumedly known PSF, so-called "classical" deconvolution; the method is then extended to the joint estimation of the object and the PSF, called here "myopic" deconvolution.

3.1 Deconvolution with known PSF

Following a probabilistic approach, called maximum *a posteriori* [MAP] [16],

the deconvolution problem can be stated as follows: we look for the most likely object \mathbf{o} given the observed image \mathbf{i} . This reads:

$$\begin{aligned} \hat{\mathbf{o}}_{\text{map}} &= \arg \max_{\mathbf{o}} p(\mathbf{o}|\mathbf{i}) = \\ &= \arg \max_{\mathbf{o}} p(\mathbf{i}|\mathbf{o}) \times p(\mathbf{o}) = \\ &= \arg \min_{\mathbf{o}} [J_n(\mathbf{o}) + J_o(\mathbf{o})]. \end{aligned} \quad (2)$$

The criterion to be minimised, $J = J_n + J_o$, is composed of a first term ($J_n = -\ln p(\mathbf{i}|\mathbf{o})$) accounting for the noise statistics in the image, plus a second term ($J_o = -\ln p(\mathbf{o})$) which allows to use the *a priori* knowledge we have on the object. This last term, of course, is a function of the type of object being observed. The choice of J_o for planetary-type objects is discussed in the Section 3.1.2.

If no prior knowledge is available, one can still use the previous equations with $p(\mathbf{o}) = 1$. One therefore only maximises $p(\mathbf{i}|\mathbf{o})$, also called likelihood of the data, to obtain a maximum-likelihood solution. In this case the criterion is only constituted of the term J_n .

3.1.1 Maximum likelihood with photon noise

If the image is corrupted solely by photon noise, the maximum likelihood [ML] solution minimises the following criterion, directly derived from the expression of Poisson statistics:

$$\begin{aligned} J_n^{\text{poisson}}(\mathbf{o}) &= -\ln p(\mathbf{i}|\mathbf{o}) = \\ &= \sum_r (\mathbf{h} * \mathbf{o})(r) - \mathbf{i}(r) \ln[(\mathbf{h} * \mathbf{o})(r)]. \end{aligned} \quad (3)$$

The Richardson-Lucy algorithm [RL] [17, 18] is an iterative numerical method which converges towards the global minimum of J_n^{poisson} .

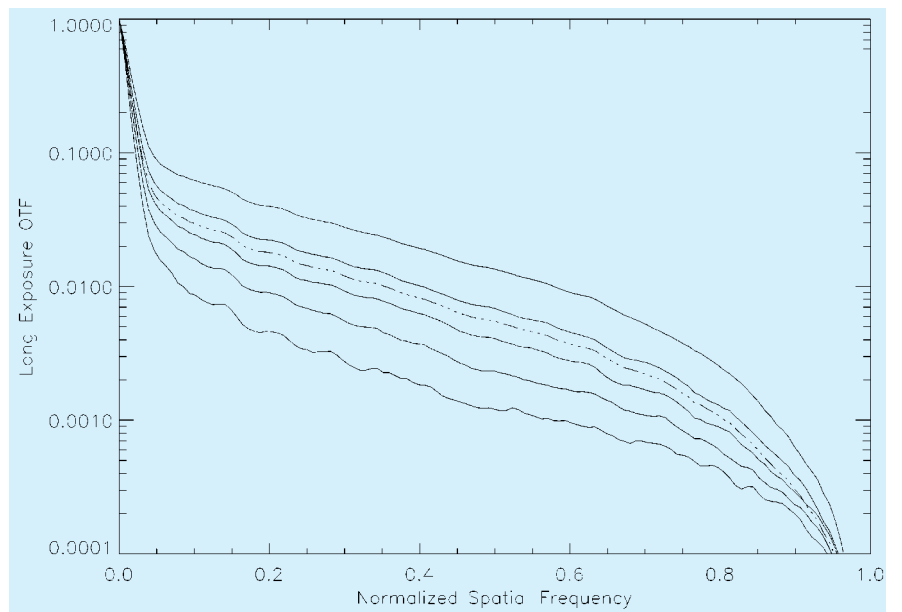


Figure 2: The OTFs are estimated for the following seeing values: from top to bottom, 0.65, 0.73, 0.79, 0.85 and 0.93 arcsec. The corresponding SRs are respectively: 3.8%, 2.1%, 1.3%, 0.8% and 0.4%. The mean OTF is also drawn (dashed line).

It is however well known that the restoration of the object using the sole data is an unstable process (see in particular Refs. [19] and [16] for reviews). The noise is highly amplified in the solution. Of course, one can stop the RL before convergence to limit the noise amplification but in this case the solution is poorly defined. For sure, it is no more the minimum of any criterion. A better solution is to regularise the problem with an adequate object prior as proposed in Section 3.1.2.

3.1.2 Edge preserving regularised deconvolution

In the MISTRAL algorithm, we consider a white non-stationary Gaussian noise in the image, which is a good approximation of a mix of photon and background (detector or sky-background) noise. Furthermore, the deconvolution is regularised by an object prior particularly adapted for planetary-like objects. This prior avoids the usual ringing artefacts [20] given by standard deconvolution techniques on such sharp edge objects [21, 8]. The criterion to be minimised is:

$$J(\mathbf{o}) = J_n(\mathbf{o}) + J_o(\mathbf{o}) = \sum_r \frac{1}{2\sigma^2(r)} (i(r) - (\mathbf{o} * \mathbf{h})(r))^2 + J_o(\mathbf{o}), \quad (4)$$

where $\sigma^2(r)$ is the image thresholded to the background noise variance. In the absence of background noise, this expression of J_n is actually a first-order development of Eq. 3. The regularisation term is defined as:

$$J_o(\mathbf{o}) = \mu \sum_r \left[\left(\frac{\Delta \mathbf{o}(r)}{\delta} \right) - \ln \left(1 + \frac{\Delta \mathbf{o}(r)}{\delta} \right) \right], \quad (5)$$

where $\Delta \mathbf{o}(r) = \sqrt{\Delta_x \mathbf{o}(r)^2 + \Delta_y \mathbf{o}(r)^2}$, $\Delta_x \mathbf{o}$ and $\Delta_y \mathbf{o}$ are the object finite difference gradients along x and y respectively.

This regularisation, called $L_1 - L_2$, is an isotropic version of the expression suggested by Brette [22]. The global factor μ and the threshold δ have to be adjusted according to the noise level and the structure of the object. This is currently done by hand but an automatic procedure is under study.

We use a fast conjugate gradient method [23] to minimise the global criterion J given in Eq. 4. This method is well adapted since the so-defined criterion is convex. An additional positivity constraint is used in MISTRAL, it is enforced with a reparameterisation method ($\mathbf{o} = \mathbf{a}^2$) [24] where \mathbf{a} are the new parameters used in the minimisation.

3.2 Myopic deconvolution

As mentioned in Section 2, the true residual PSF is seldom available. MIS-

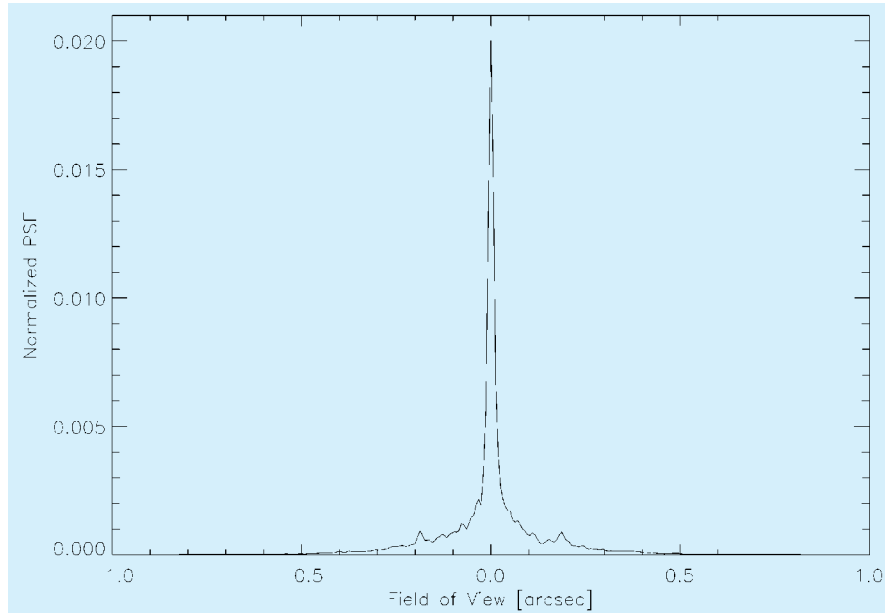


Figure 3: VLT-NAOS PSF at $0.5 \mu\text{m}$, for 0.73 arcsec seeing and a guide star magnitude $m_V = 11$. The PSF is normalised to its Strehl Ratio $SR \approx 2.1\%$.

TRAL has the ability to estimate both the object and PSF from the image and some imprecise PSF measurement. The Eqs. 2 and 4 can indeed be generalised, in the same probabilistic framework, to the case of a joint estimation of $[\mathbf{o}, \mathbf{h}]$. One obtains:

$$\begin{aligned} [\hat{\mathbf{o}}, \hat{\mathbf{h}}] &= \arg \max_{\mathbf{o}, \mathbf{h}} \rho(\mathbf{o}, \mathbf{h} | \mathbf{i}) = \\ \arg \max_{\mathbf{o}, \mathbf{h}} \rho(\mathbf{i} | \mathbf{o}, \mathbf{h}) \times \rho(\mathbf{o}) \times \rho(\mathbf{h}) &= \quad (6) \\ \arg \min_{\mathbf{o}, \mathbf{h}} [J_n(\mathbf{o}, \mathbf{h}) + J_o(\mathbf{o}) + J_h(\mathbf{h})]. & \end{aligned}$$

The myopic criterion is given by Eqs. 4 and 5, now a function of \mathbf{o} and of \mathbf{h} , plus an additional term $J_h = -\ln \rho(\mathbf{h})$ which accounts for the knowledge, although partial, available on the PSF. Assuming stationary Gaussian statistics for the PSF, J_h reads:

$$J_h(\mathbf{h}) = \frac{1}{2} \sum_f \frac{|\tilde{\mathbf{h}}(f) - \tilde{\mathbf{h}}_m(f)|^2}{PSD_h(f)}, \quad (7)$$

where $\tilde{\mathbf{h}}_m = E[\tilde{\mathbf{h}}]$ is the mean OTF, and $PSD_h = E[|\tilde{\mathbf{h}}(f) - \tilde{\mathbf{h}}_m(f)|^2]$ is the associated spatial Power Spectral Density [PSD].

Such a regularisation obviously ensures that the actual OTF is close to the mean OTF with respect to error bars given by the PSD, which characterises the fluctuations around the mean. In practice, the mean PSF and the PSD are estimated by replacing, in their definitions, the expected values ($E[\cdot]$) by an average on the different images recorded on the unresolved star. Ideally one would want to estimate the PSF from the wavefront sensing data [10, 25] which would avoid the errors due to seeing fluctuations. But even in this case, the myopic approach can be interesting to account for the PSF uncertainties due to constant aberration cali-

bration errors [9] or to the wavefront sensing noise for faint stars.

Note that the new criterion is convex in \mathbf{o} for a given \mathbf{h} , convex in \mathbf{h} for a given \mathbf{o} but it is not convex on the whole parameter space. However, it is possible to use starting points that are close to the global minimum, and we did not encounter minimisation problems with the conjugate gradient method. A positivity constraint is also used on the PSF ($\mathbf{h} = \mathbf{b}^2$).

4. Deconvolution of Simulated VLT-NAOS Images

The application of MISTRAL to the simulated VLT-NAOS visible image presented in Section 2 is discussed here.

Figure 4 shows the results obtained in the ideal case of a classical deconvolution using the true PSF. The deconvolution obtained with MISTRAL at convergence (360 iterations) of the minimisation of Eq. 4 is compared to the RL estimation stopped respectively at 1000, 6830 and 50,000 iterations. In each case a log-scale version of the restored object is shown in order to check the detection of the faint stars in the background.

A quantitative measurement of the restoration quality can be given in terms of distance to the true object, rms value expressed in photons/pixel and computed on the full field of view. The distance is 5150 photons/pixel for the MISTRAL estimate, and respectively 11,800, 9900 and 13,900 photons/pixel for the RL cases. The evolution of the distance with the computation time is given in Figure 5. The estimate obtained with 6830 iterations and shown in Figure 4 therefore corresponds to the best RL estimate. The starting point is always the image thresholded to a slightly positive level for implementation

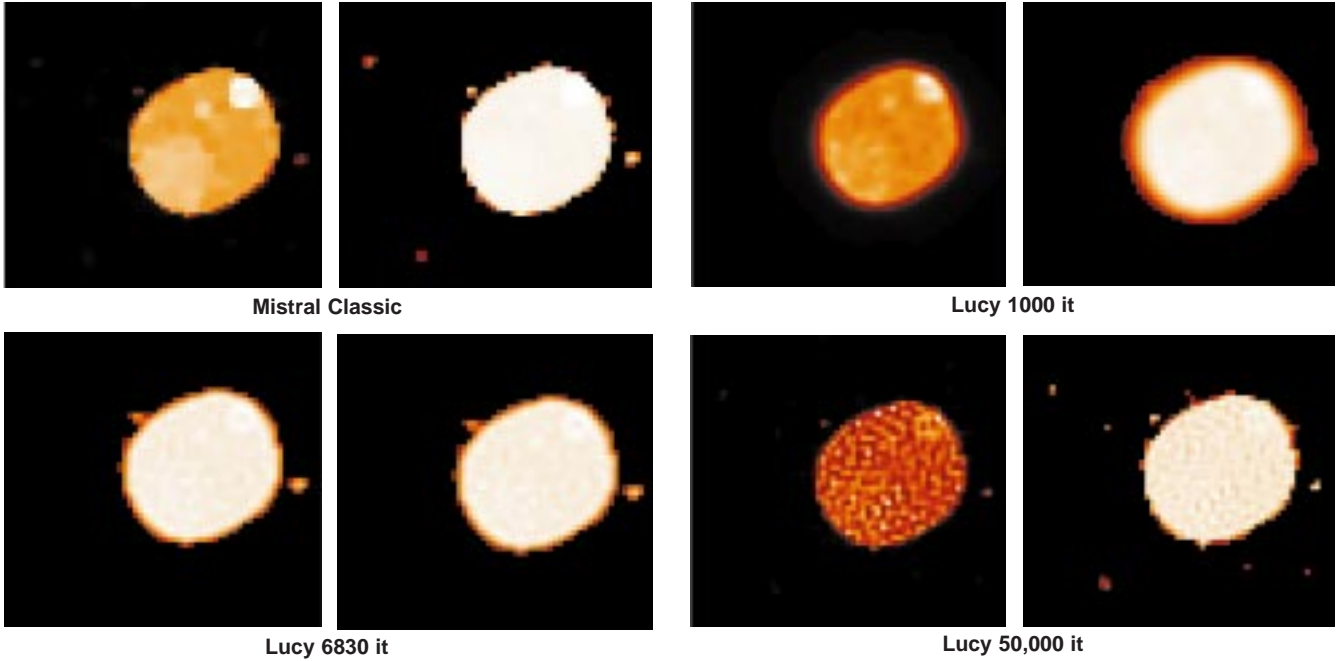


Figure 4: Classical deconvolution with MISTRAL and RL estimates with 1000, 6830 and 50,000 iterations. The PSF is the true PSF. The deconvolution is performed on the 0.8 arcsec field of view but only a 0.4 arcsec subfield is displayed. In each case we show the corresponding log-scale map (right-hand side panel in each pair of images). The distance to the true object is 5150 photons/pixel with MISTRAL and respectively 11,800, 9900 and 13,900 photons/pixel for the RL cases.

of the positivity. The RL estimate never reaches the distance obtained with MISTRAL and diverges for a large number of iterations. It goes from a low-resolution estimate with ringing artefacts to a very noisy one. The restoration quality is obviously much higher with our regularised algorithm. The global photometry is very precisely restored. The stars in the background are well detected and only slightly smoothed. This large dynamic is permitted by a good model of the image noise. Note also that MISTRAL reaches convergence in a quite reasonable amount of time (≈ 390 s and 360 iterations), roughly the same time required for RL to reach its best estima-

tion (≈ 330 s and 6800 iterations). Note also that MISTRAL is able to both restore the edge of the object and the structures on the surface.

We then consider the case of a poor estimation of the PSF. We recall that the image was obtained with a PSF corresponding to a 0.73 arcsec seeing. We assume that 5 images of an unresolved star were recorded shortly before or after. The seeing is supposed to be unstable and the seeing is actually 0.65, 0.73, 0.79, 0.85 and 0.93 arcsec respectively for each of these calibration images. The OTF estimates are shown in Figure 2 as well as the mean OTF. Since it can be difficult to estimate precisely the seeing conditions to select

the correct OTF, one may want to use a classical deconvolution assuming that the true OTF is the mean OTF. The result obtained with MISTRAL with this assumption is shown in Figure 6. Despite the fact that the mean OTF is close to the true one ($SR = 1.7\%$ instead of 2.1%), the restoration is poor: artefacts on the surface, apparent diameter underestimated, no detection of the surrounding stars. The distance to the true object is large ($\approx 23,000$ photons/pixel). The other approach is to use MISTRAL in the myopic mode (minimisation at convergence of Eq. 6) with the same mean OTF and a PSD which is nothing but the variance estimated out of these 5 OTF measurements for each spatial frequency. The restoration is very similar to that obtained with the true PSF. The distance to the true object is ≈ 6800 photons/pixel. Note however that part of the dynamic is lost. Only the two brightest stars are detected. The computation time required in the myopic case is ≈ 1900 s (1600 iterations) which is still quite reasonable.

5. Deconvolution of Experimental ADONIS Data

ADONIS, the AO system mounted on the 3.6-m telescope of the La Silla observatory, has been routinely used by the ESO community since 1993. The wavefront distortions of the visible incoming light are measured using one of the two Shack-Hartmann wavefront sensors (WFS). The 52-actuators deformable mirror and tip-tilt mirror control is performed by a modal optimisation. ADONIS is the only AO system providing an imaging facility in the 1–5 μm range via two NIR cameras. The plane-

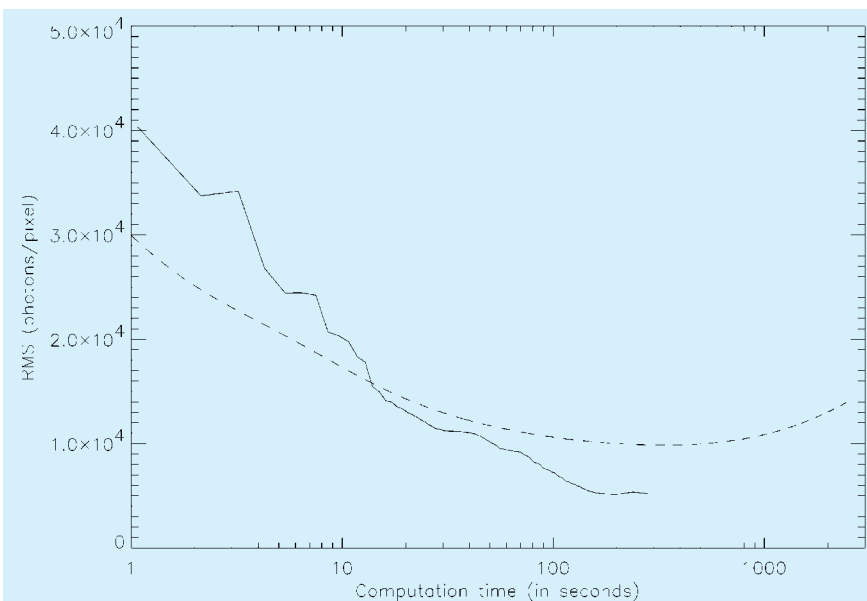


Figure 5: Distance to the true object, rms value expressed in photons/pixel, versus computation time: MISTRAL (solid line), RL (dashed line).

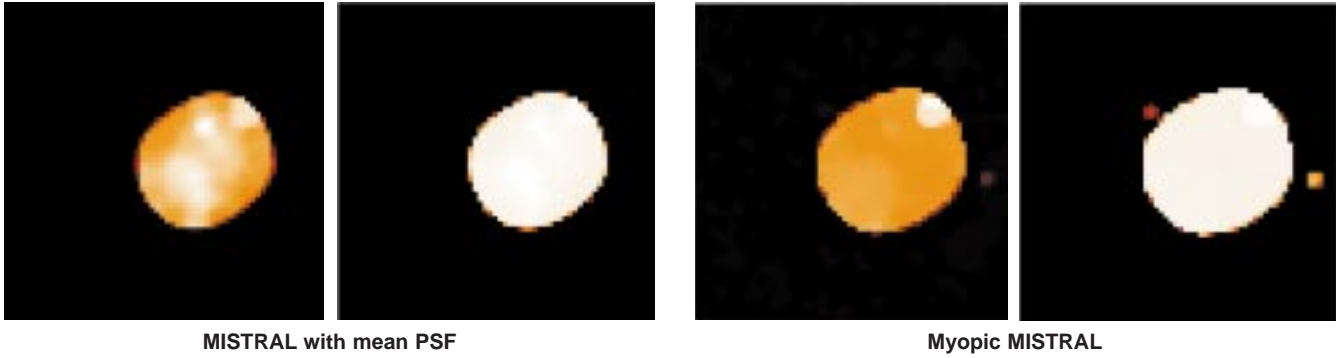


Figure 6: MISTRAL classical deconvolution with mean PSF considered as the true PSF and myopic deconvolution. In each case we show the corresponding log-scale map. The deconvolution is performed on the 0.8 arcsec field of view but only a 0.4 arcsec sub-field is displayed. The distance to the true object is respectively 23,000 and 6800 photons/pixel (see Section 4).

tary observations presented below have been performed without prefocal optics using broad-band filters.

5.1 Monitoring of Io's volcanism

Io's volcanic activity, attributed to internal heating due to tidal effects between Jupiter and Io, was first discovered from space with Voyager 1 and 2 in 1979. They have shown the presence of active volcanic centres, called hot spots, detectable by their IR emission. Since then, and because of the increase in IR detector sensitivity, Io's variable volcanos of the Jupiter-facing hemisphere have been studied by ground-based observations when Io is located in the shadow of Jupiter [27]. Since October 1996, ADONIS AO system coupled with its COMIC thermal camera (CEA/LIR/LETI detector, 128×128 , 100 mas/pixel) has been used to monitor Io's volcanic activity [28]. Observations performed with a L' broad-band filter ($\lambda_c = 3.8 \mu\text{m}$) using the satellite itself as reference (angular size ~ 1.0 arcsec, $m_v \sim 5$) allow a complete mapping of its surface. In this spectral range, the AO correction is quite efficient and the typical SR obtained is around 45% with a 0.8 arcsec seeing.

An AO corrected image and the corresponding PSF are presented in Figure 7. Only the bright Loki hot spot is detected on the AO corrected image. A deconvolution is required to study other structures. In addition to the residual blur, the image incorporates a rather uniform high-level background emission produced by the sky and the bench optical elements [29] and a variable and inhomogeneous background modulated by the AO correction [30]. A good background subtraction is of course important for the deconvolution.

We present in Figure 8 two consecutive images of Io's Jupiter-facing hemisphere taken in September 1998 and processed with MISTRAL [31]. We used the myopic mode to account for seeing variations. Loki, well-known hot spot located on the Jupiter-facing hemisphere, is quite active and surrounded by secondary outbursts. Standard deconvolution processes cannot be applied on these data. Indeed, in the absence of edge-preserving regularisation term, the whole energy of the disk tends to be concentrated in the bright Loki feature. Our observations are well correlated to, and complement those, made by

Galileo/NIMS spectrocamera [26] (see Fig. 8). The coupling of AO system with a thermal camera and the use of a specific deconvolution process for planetary objects, such as MISTRAL, is very promising for our understanding of Io's volcanism which can only be accomplished by a frequent monitoring of its activity.

5.2 Study of the Uranian system

Uranus has been observed with broad-band filters (J,H,K) using the SHARPII+ camera (Rockwell NICMOS3 detector, 1–2.5 μm , 100 mas/pixel) on May 2, 1999. These observations have been performed thanks to the capability of the Shack-Hartmann WFS to analyse the wavefront on an extended object. Because of the relatively small angular size of the planet (2.6 arcsec) and the excellent seeing condition (0.5 arcsec and very stable), the correction quality was high and we got a SR of 48% in K band (2.2 μm). The centroid position error, in each sub-pupil, is however higher on extended objects, hence a degraded AO performance on such extended objects. The image of an unresolved star is therefore a biased measurement of the

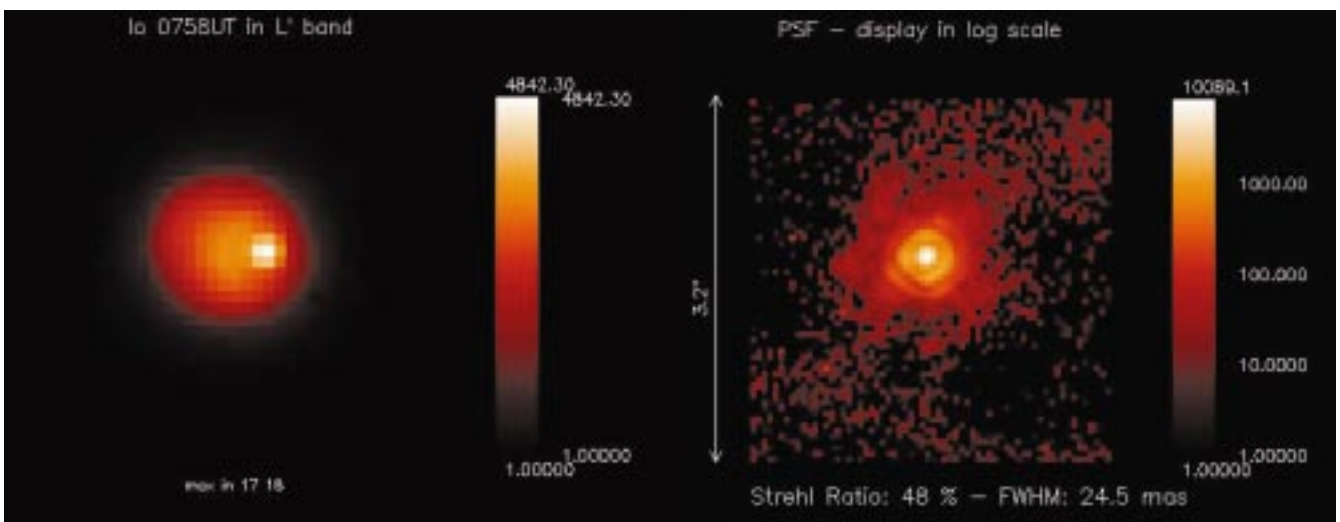


Figure 7: ADONIS image of Io and a log-scale representation of the corresponding PSF. Only the bright Loki hot spot is detected on the Io's disk.

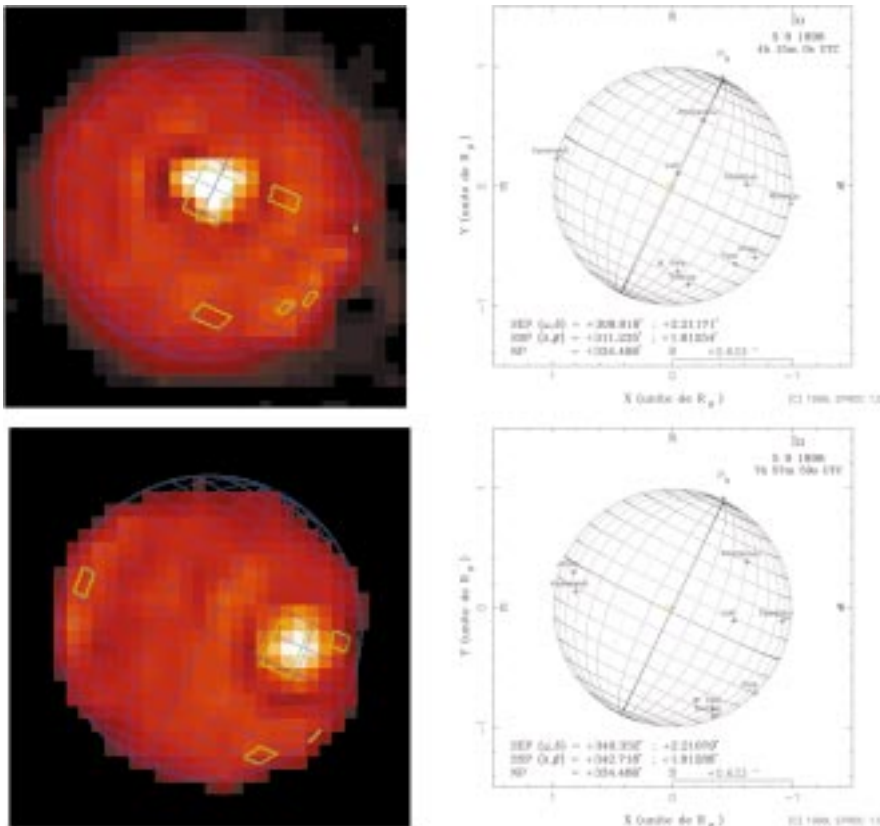


Figure 8: Two consecutive images of the Jupiter-facing hemisphere of Io observed with ADONIS/COMIC in L' band and processed with MISTRAL. The green boxes correspond to the projection of the hot spots detected by Galileo/NIMS during the first four orbits [26]. The right panel indicates the geometry of Io at the date of the observation and the name of the known hot spots (courtesy Bureau des Longitudes). See Section 5.

PSF and a myopic deconvolution method is definitely necessary to restore the initial sharpness of the images. Figure 9 displays a set of data after deconvolution with MISTRAL. In J (1.2 μm) and H (1.6 μm) bands, the planetary disk is not uniform as observed in the visible and shows bright polar haze distributed along a latitude. In K band, due to the methane atmospheric absorption band, the planet is dark and the brightest feature is the Epsilon ring with its longitudinal anomaly.

J and H band (Fig. 10), one can see the Epsilon ring and also some innermost ones. The exterior satellites Ariel, Miranda and Puck can be detected with standard deconvolution such as RL. But the myopic deconvolution process also reveals the presence of the innermost satellites, Portia, Rosalind, Bianca and Juliet (see Fig. 10) which have been discovered by Voyager 2 in 1986 and never re-observed since then. After these first successful observations, the monitoring of Uranus and its environment will continue. The AO system fa-

cility and the accurate MISTRAL deconvolution method will allow us to study the atmospheric activity of the planets, the colour and composition of the rings. The comparison of the positions of the faintest satellites with ephemerides will also better constrain physical parameters (body masses, flattening factor . . .) and to elaborate a more accurate analytical theory of the satellite motion [32].

6. Conclusion

MISTRAL is a myopic deconvolution algorithm particularly adapted for AO corrected images of astronomical objects. It accounts for the noise in the image, for the presence of sharp structures in the object and for the fact that the PSF is usually not perfectly known. Its ability to provide high photometric precision estimates with a quite reasonable computation time has been illustrated on simulated data. The simulation conditions correspond to a VLT-NAOS observation in the visible. Since the system is optimised in the near IR, the correction quality in the visible is low ($SR \approx 2\%$ here). Even in such severe conditions, a diffraction-limited restoration is obtained.

MISTRAL has also been applied to ADONIS images of Io in the thermal domain, and images of Uranus in the near IR. In addition to the bright hot spot Loki, secondary outbursts were observed on Io's Jupiter-facing hemisphere. Such observations are very promising for our understanding of Io's volcanism which can only be accomplished by frequent monitoring of its activity. Concerning Uranus, the structures of the rings and its innermost satellites have been successfully detected. We will continue a monitoring of Uranus and its environment. Solar-system studies (atmospheric activity of the planets, colour and composition of the rings, position of the faint satellites) require high-resolution and high-photometric-precision data. These can be ob-

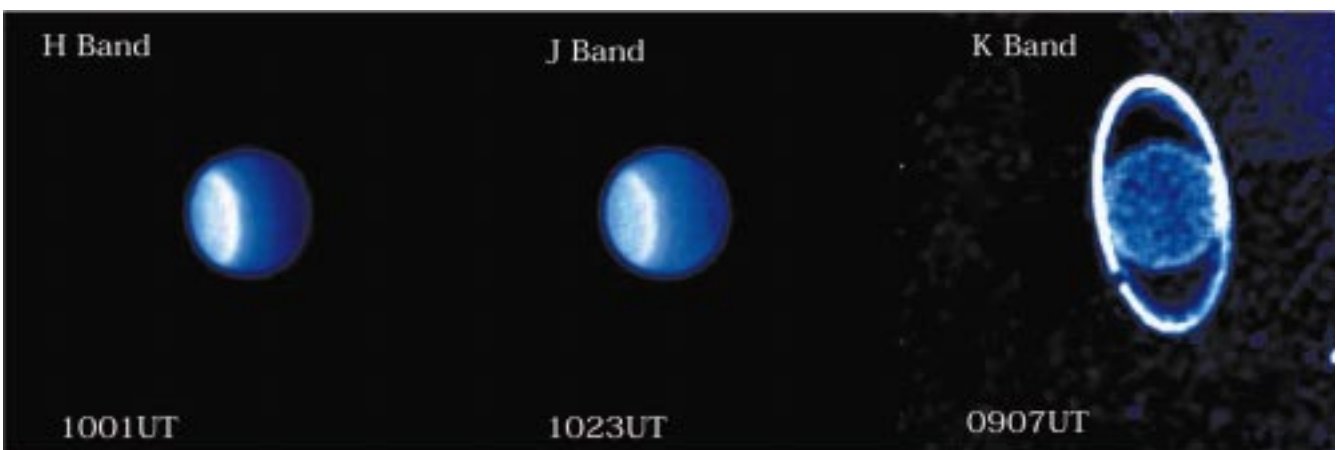


Figure 9: Uranus observed in May 1999 (north is down, east is left) after deconvolution by MISTRAL. In J and H bands, the hazy atmospheric regions are clearly visible around the pole. In K band, the methane atmospheric band absorbs the solar light and the bright feature observed is the Epsilon ring and its longitudinal anomaly.

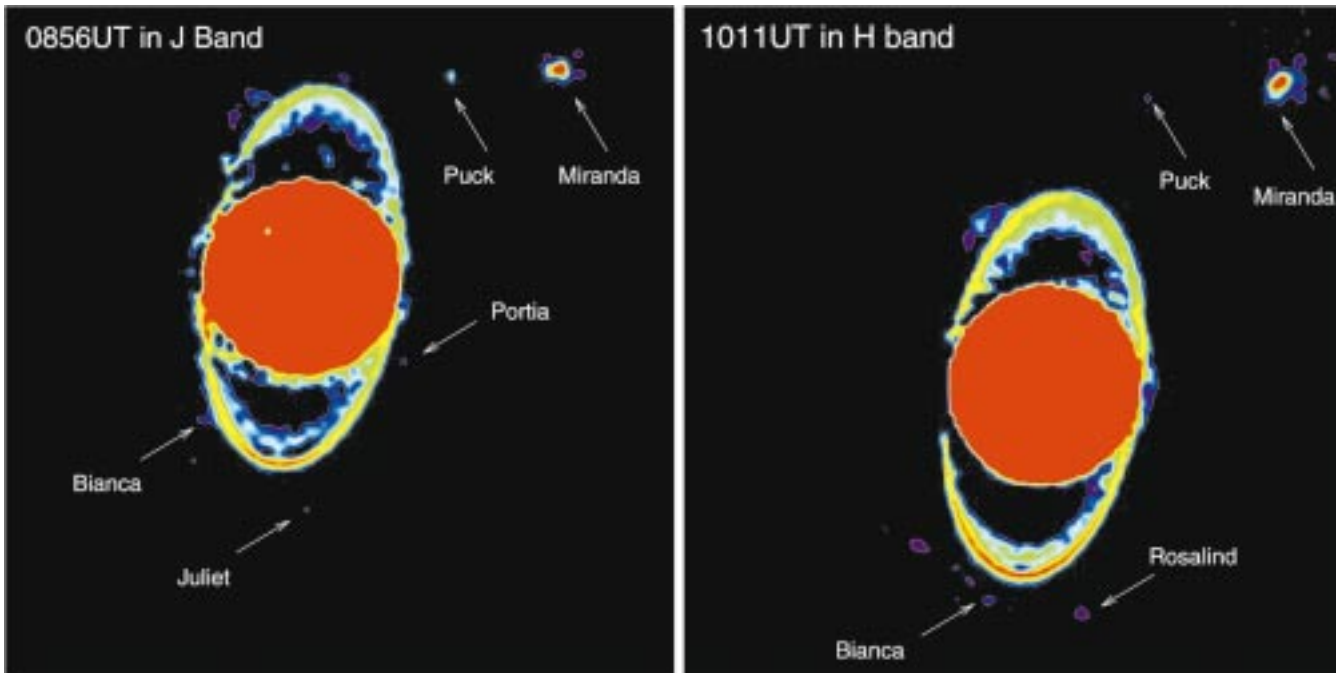


Figure 10: Logarithmic display of the MISTRAL images (north is up and east is left) showing the lowest intensity levels in the J and H images. Innermost rings and faintest satellites (first observed with Voyager in 1986) are also detected.

tained with large telescope AO observations in conjunction with a high-precision deconvolution technique.

7. Acknowledgements

The authors thank Gérard Rousset, Vincent Michau, Claude and François Roddier, Jérôme Idier and Guy Le Besnerais for many fruitful discussions. We are indebted to ESO-3.6-m support team, in particular the Telescope Operators for their assistance during these difficult and unusual planetary object observations.

References

- [1] J.W. Hardy, J. E. Lefevbre, and C.L. Koliopoulos, "Real time atmospheric compensation", *J. Opt. Soc. Am.* **67**, 360–369 (1977).
- [2] G. Rousset, J.-C. Fontanella, P. Kern, P. Gigan, F. Rigaut, P. Léna, C. Boyer, P. Jagourel, J.-P. Gaffard, and F. Merkle, "First diffraction-limited astronomical images with adaptive optics", *A&A* **230**, 29–32 (1990).
- [3] *Adaptive Optics in Astronomy*, F. Roddier, ed., (Cambridge University Press, 1999).
- [4] F. Rigaut, G. Rousset, P. Kern, J.-C. Fontanella, J.-P. Gaffard, F. Merkle, and P. Léna, "Adaptive optics on a 3.6-m telescope: results and performance", *A&A* **250**, 280–290 (1991).
- [5] M.C. Roggemann and C.L. Matson, "Power spectrum and Fourier phase spectrum estimation by using fully and partially compensating adaptive optics and bispectrum postprocessing", *J. Opt. Soc. Am. A* **9**, 1525–1535 (1992).
- [6] J.M. Conan, P.Y. Madec, and G. Rousset, "Image formation in adaptive optics partial correction", in *Active and Adaptive Optics*, (Garching, Germany, 1993).
- [7] J.-M. Conan, "Étude de la correction partielle en optique adaptative", Ph.D. thesis, Université Paris XI Orsay, 1994.
- [8] J.-M. Conan, T. Fusco, L. Mugnier, E. Kersalé, and V. Michau, "Deconvolution of adaptive optics images with imprecise knowledge of the point spread function: results on astronomical objects", in *Astronomy with adaptive optics: present results and future programs*, (Sonstofen, 1998).
- [9] T. Fusco, J.-P. Véran, J.-M. Conan, and L. Mugnier, "Myopic deconvolution method for adaptive optics images of stellar fields", *A&A Suppl. Ser.* **134**, 1–10 (1999).
- [10] J.-P. Véran, F. Rigaut, H. Maître, and D. Rouan, "Estimation of the adaptive optics long exposure point spread function using control loop data", *J. Opt. Soc. Am. A* **14**, 3057–3069 (1997).
- [11] J.-M. Conan, L. M. Mugnier, T. Fusco, V. Michau, and G. Rousset, "Myopic Deconvolution of Adaptive Optics Images using Object and Point Spread Function Power Spectra", *Appl. Opt.* **37**, 4614–4622 (1998).
- [12] G. Rousset et al., "Design of the Nasmyth Adaptive Optics System (NAOS) of the VLT", in *Astronomical Telescopes & Instrumentation*, D. Bonaccini and R. K. Tyson, eds., 3353 (Kona, Hawaii, 1998).
- [13] J.C. Christou, "Deconvolution of adaptive optics images", in *ESO/OSA topical meeting on astronomy with adaptive optics present results and future programs*, (1998).
- [14] E. Tessier, "Image quality with current adaptive optics instruments", *A&A Suppl. Ser.* **125**, 581–593 (1997).
- [15] J.-M. Conan, D. Mouillet, E. Gendron, and G. Rousset, "NAOS analysis report Issue 2.0", Rapport Technique VLT-TRE-NAO-11650-1-000000-0002, ONERA (1999), contract ESO.
- [16] G. Demoment, "Image Reconstruction and Restoration: Overview of Common Estimation Structures and Problems", *IEEE Trans. Acoust. Speech Signal Process.* **37**, 2024–2036 (1989).
- [17] W.H. Richardson, "Bayesian-based iterative method of image restoration", *J. Opt. Soc. Am.* **62**, 55–59 (1972).
- [18] L. B. Lucy, "An iterative technique for rectification of observed distributions", *Ap.J.* **79**, 745–754 (1974).
- [19] D. M. Titterton, "General structure of regularization procedures in image reconstruction", *A&A* **144**, 381–387 (1985).
- [20] J.-P. Véran, "Estimation de la réponse impulsionnelle et restauration d'image en optique adaptative – Application au système d'optique adaptative du Télescope Canada-France-Hawaii", Ph.D. thesis, Ecole Nationale Supérieure des Télécommunications, 1997.
- [21] L. M. Mugnier, J.-M. Conan, T. Fusco, and V. Michau, "Joint Maximum a Posteriori Estimation of Object and PSF for Turbulence Degraded Images", in *Bayesian Inference for Inverse problems*, **3459**, 50–61 (San Diego, CA (USA), 1998).
- [22] S. Brette and J. Idier, "Optimized Single Site Update Algorithms for Image Deblurring", in *Proceedings of the International Conference on Image Processing*, p. 65–68 (Lausanne, Switzerland, 1996).
- [23] Groupe Problèmes Inverses, "GPAV: une grande œuvre collective", internal report, Laboratoire des Signaux et Systèmes, CNRS/Supélec/Université Paris-Sud (1997).
- [24] E. Thiébaud and J.-M. Conan, "Strict a priori constraints for maximum-likelihood blind deconvolution", *J. Opt. Soc. Am. A* **12**, 485–492 (1995).
- [25] S. Harder, "Reconstruction de la réponse impulsionnelle du système d'optique adaptative ADONIS a Dartir des mesures de son analyseur de surface d'onde et Étude photométrique de la variabilité des étoiles YY Orionis", Ph.D. thesis, Université Joseph Fourier, Grenoble 1, 1999.
- [26] R. Lopes-Gautier, A. Davies, R. Carlson, W. Smythe, L. Kamp, L. Soderblom, F. E.

- Leader, and R. Mehlman, "Hot spots on Io: Initial results from Galileo's near infrared mapping spectrometer", *Geophys. Res. Lett.* **24**, 2439 (1997).
- [27] J. R. Spencer, J. A. Stansberry, C. Dumas, D. Vakil, R. Pregler, M. Hicks, and K. Hege, "History of high-temperature Io volcanism: February 1995 to May 1997", *Geophys. Res. Lett.* **24**, 2451 (1997).
- [28] F. Marchis, R. Prangé, and J.C. Christou, "Adaptive Optics mapping of Io's volcanism in the thermal IR", *Icarus* (1999), submitted.
- [29] D. Le Mignant, E. Gendron, and F. Marchis, "The ESO ADONIS adaptive optics system: Study of the 3-5 μ m background emissivity", in *ESO conference and workshop proceedings* **56**, 575 (Garching, Germany, 1998).
- [30] H. Geoffray, "Thermal background blurring on ADONIS system", in *ESO conference and workshop proceedings* **56**, 531 (Garching, Germany, 1998).
- [31] R. Prangé, F. Marchis, and T. Fusco, "Mapping and monitoring of Io's hot spots by use of the ESO Adaptive Optics system.", in *31st Annual Meeting of the DPS*, (Padova, Italy, 1999).
- [32] F. Marchis, J. Berthier, P. Descamps, T. Fusco, R. Prangé, and T. Sekiguchi, "Ground-based high resolution observations of the Uranian system in the near IR", in *31st Annual Meeting of the DPS*, (Padova, Italy, 1999).

A New Look at the Sombrero Galaxy



This image of Messier 104, also known as Sombrero Galaxy, because of its particular shape, was obtained with FORS1 at VLT Antu on January 30, 2000. The colour image was made by a combination of three CCD images obtained by Peter Barthel from the Kapteyn Institute at Groningen, Netherlands. He and Mark Neeser, also from the Kapteyn Institute, produced the composite images. The "Sombrero" is notable for its dominant nuclear bulge, composed primarily of old stars, and its nearly edge-on disk composed of stars, gas and intricately structured dust. The complexity of this dust and the high resolution of this image are most apparent directly in front of the bright nucleus, but it is also evident as dark absorbing lanes throughout the disk.